ORIGINAL RESEARCH ARTICLE

Influence of Surface Mechanical Attrition Treatment Parameters on Microstructure and Residual Stress of Mg5Zn0.2Ca Alloy

Nilesh K. Kumbhar, Vikesh Kumar, and Santosh S. Hosmani

Mg5Zn0.2Ca is a promising alloy for medical tools owing to its excellent biocompatibility and biodegradability. This study presents the impact of surface mechanical attrition treatment (SMAT) parameters, explicitly colliding balls velocity (1, 5, and 10 m/s), and surface coverages (500, 1000, and 2000%), on the microstructure, hardness, and residual stress. SMAT forms a layer with a gradient in hardness, crystallite size, and twins. The surface hardness, which ranges between 68 and 118 $HV_{0.05}$, increases with increased ball velocity and surface coverage. High ball velocity (10 m/s) and surface coverage (2000%) induce high compressive residual stress of about -175.5 MPa at $\sim$600 μm depth. The specimens SMATed with a ball velocity of 5 m/s exhibit the higher surface compressive residual stress for all surface coverages. The maximum compressive residual stress of about -153.5 MPa is observed at the surface for the specimens SMATed at 5 m/s ball velocity and 500% coverage. The overall analysis reveals that the specimen treated at 10 m/s ball velocity and 2000% surface coverage exhibits the most refined grain structure, finely and densely distributed twins, maximum SMAT-induced thickness ($\sim$3000 μm), highest surface hardness ($\sim$2.1 times the non-SMATed specimen's hardness), and maximum compressive residual stress.

1. Introduction

MgZnCa magnesium alloy is a promising material for medical devices such as orthopedic implants, cardiovascular stents, and surgical instruments due to its excellent biocompatibility and biodegradability (Ref 1, 2). Most studies focused on optimizing the chemistry of this alloy to tune the properties. Adding a small quantity of Ca to magnesium alloys enhances ductility (Ref 3). However, a higher amount of Ca (> 0.2 wt.%) increases the likelihood of Mg_2Ca_2 formation at grain boundaries, decreasing their strength (Ref 3). Adding Zn enhances the grain boundary resilience of Ca-containing alloys, increasing cohesion between grains and reducing the

Nilesh K. Kumbhar, Vikesh Kumar, and **Santosh S. Hosmani**, Department of Metallurgical Engineering and Materials Science, Indian Institute of Technology Indore, Indore 453552, India. Contact e-mail: sshosmani@iiti.ac.in.

formation of such Ca-rich clusters at grain boundaries (Ref 4). Incorporating Zn up to 6 wt.% enhances mechanical properties and increases the degradation resistance of the alloy; however, when Zn content exceeds 6 wt.%, the emergence of the $Mg_{51}Zn_{20}$ phase triggers a faster degradation rate (Ref 5). Hence, Mg5Zn0.2Ca alloy (having an appropriate composition of elements) is chosen in the current study and recognized the need for further enhancement in its properties to meet the application requirements.

Most of the recent literature on MgZnCa magnesium alloy was devoted to enhancing mechanical properties (like fatigue resistance) and corrosion resistance by controlling the chemistry and microstructure of the alloy (Ref 6-10). However, the current knowledge of this alloy is limited, and its wider use is constrained by relatively low mechanical properties and high susceptibility to environmental factors (Ref 8, 11). Nanocrystalline materials can enhance these aspects (Ref 12-14). Predominantly, material failures due to wear, fretting fatigue, and fatigue fractures originate at the surface; therefore, making the surface nanocrystalline via severe plastic deformation (SPD) processes is a topic of substantial interest (Ref 15-17). Surface mechanical attrition treatment (SMAT) stands out across various SPD techniques due to its process capabilities, cost-efficient approach, and ability to control microstructure and properties. The influence of severe plastic deformation on the MgZnCa alloy surface has only been addressed in limited research articles.

Furthermore, fatigue behavior, one of the crucial properties, depends on the residual stress induced by the surface-treatments. Therefore, investigating the residual stresses generated by severe surface deformations has become a significant area of interest from an application standpoint. This study investigates

the impact of SMAT process parameters on the microstructure, hardness, and residual stress in MgZnCa alloy.

2. Methodology and Experimentation

2.1 Sample Preparation and SMAT Operation

For this study, Mg5Zn0.2Ca alloy, consisting of 5 wt.% Zn, 0.2 wt.% Ca, and the remaining Mg, was selected. Specimens with dimensions of $50 \times 50 \times 5$ mm were initially polished with silicon carbide (SiC) emery papers and subsequently with navigated alumina and diamond suspensions to prepare them for the SMAT operation. The SMAT operation was carried out using a specially constructed mechanical vibration-assisted setup. This setup, including a SMAT cabin, facilitated high-velocity impacts of hardened steel balls on the specimen surface, resulting in intense surface deformation. Table 1 shows the selected SMAT process parameters and the designations of specimens considered in this study.

The influence of ball velocity and surface coverage in the SMAT process on the Mg5Zn0.2Ca alloy was analyzed while keeping other factors like ball size (6 mm diameter) and the number of balls (32 nos.) constant for all specimens. During the SMAT process, achieving 100% surface coverage took ~12 min at 1 m/s, ~70 s at 5 m/s and ~30 s at 10 m/s of ball velocity. For example, the SMAT process took ~30 s (i.e., ~0.5 min) at ~10 m/s for 100% surface coverage (which corresponds to 1 peening intensity (PI)). However, to achieve 500% surface coverage, PI = 5 is considered (i.e., 30 s × 5 = 150 s (2.5 min) SMAT duration). Similarly, 10 and 20 PI correspond to 1000% (i.e., 5 min SMAT duration) and 2000% (i.e., 10 min SMAT duration) surface coverage, respectively. Therefore, different attrition durations were set to maintain an identical surface coverage percentage (500, 1000, and 2000%) for the three sets of specimens (Table 1).

2.2 Characterization of Samples

The specimens were initially polished with SiC papers, navigated alumina, and diamond suspensions of varying sizes (up to ~0.1 μm) and then finally with ~0.04 μm colloidal silica suspensions for microstructural examinations. Subsequently, these samples were chemically etched using a solution of 5 ml acetic acid, 5 ml distilled water, 2.3 g picric acid, and 35 ml ethanol. The etched specimens' microstructure was studied using optical and scanning electron microscopy (SEM).

The specimen's surface was further tested using x-ray diffraction (XRD), which used Cu-K$_{\alpha}$ radiation. The crystallite size of the SMATed specimens was determined through the Williamson–Hall method (Ref 18). To measure residual stress across the layer affected by SMAT, the thickness of the material was systematically reduced using mechanical polishing. The $(203)_{\alpha\text{-hcp}}$ peak ($2\theta = 90.46°$) was chosen for measurement. To quantify the residual stresses generated within the deformed layers at varying depths, the $\sin^2(\psi)$ method was employed. The Vickers microhardness measurements employed a 50 g load with a 10 s dwell time. Approximately, ten indents were randomly taken at each depth in the SMATed layer to evaluate microhardness distribution. Further, the surface roughness (R_a) values of the SMATed specimens were measured using a 2D profilometer.

3. Results

3.1 Microstructure Analysis

SEM micrograph and EDS spectra shown in Fig. 1(a), (b), (d) and (e) represent microstructural features of Mg5Zn0.2Ca alloy. Its microstructure consists of an α-Mg matrix, and secondary phase particles ($Ca_2Mg_6Zn_3$) are dispersed throughout the grain interior and boundary. A similar microstructure was reported in the literature (Ref 7, 19). The grain size of the as-cast Mg5Zn0.2Ca alloy is about 108 ± 5 μm. The literature has also reported an almost similar grain size of 114 ± 5 μm for as-cast Mg4Zn0.7Ca alloy (Ref 7).

The micrographs obtained using optical microscopy (Fig. 2 and 3) help reveal various microstructural features because of the different responses by these features to the etching solution. Figure 2 shows optical micrographs of Mg5Zn0.2Ca alloy, which is SMATed with different ball velocities and surface coverages. For specimens SMATed at 10 m/s ball velocity (SA7, SA8 and SA9), fine and densely distributed twins are observed compared to the other specimens. Such microstructural features cause darker contrast in the micrographs (due to the higher response to the etching solution) (Fig. 2g–i) versus (Fig. 2a–c). The darker spots in the optical micrographs indicate the presence of β-phase, especially at grain boundaries. Figure 3(a), (b) and (c) shows the twins' distribution from the treated surface to the core for SA3, SA6 and SA9. Other specimens also exhibit similar behavior in terms of the distribution of twins. SA9 (Fig. 3c) exhibits a dense distribution of fine twins near the treated surface (darker contrast is visible

Table 1 Specimen designations and SMAT process parameters

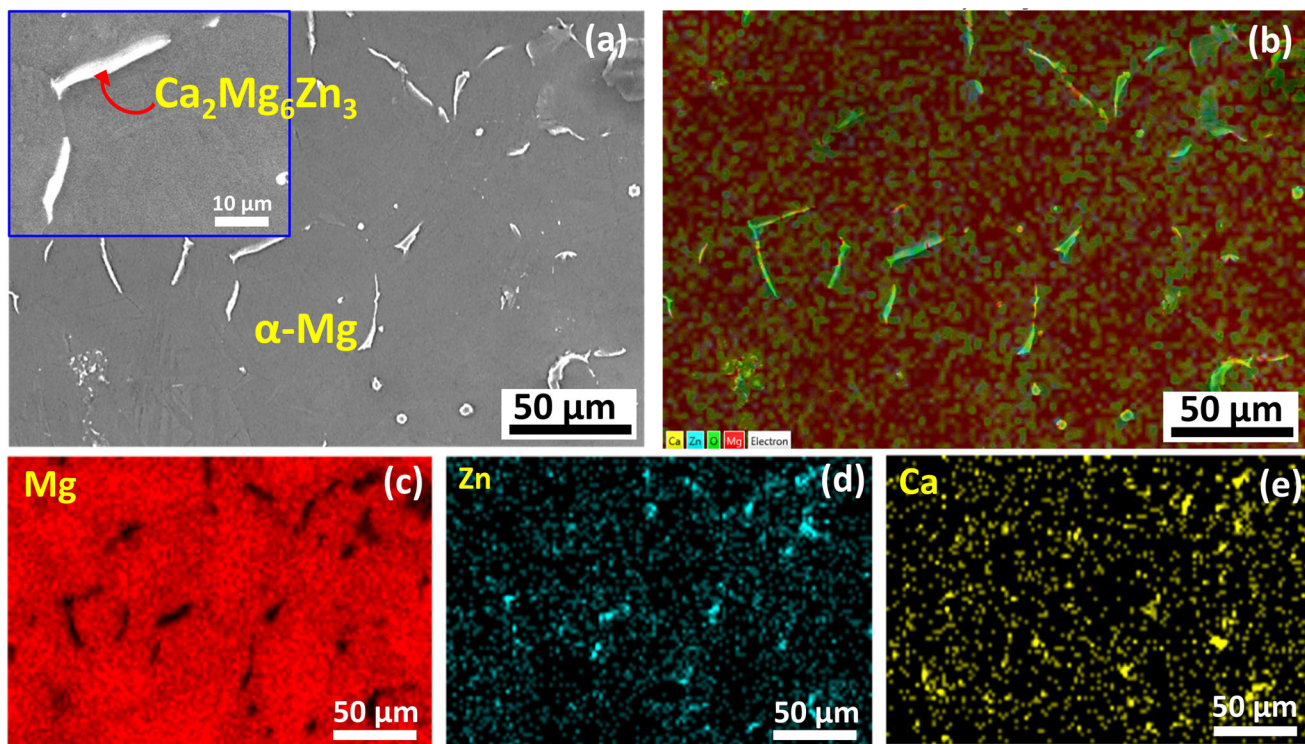| Sample condition	Ball velocity, m/s	Total coverage, %	SMAT duration, min
SA1	1	500	60
SA2		1000	120
SA3		2000	240
SA4	5	500	6
SA5		1000	12
SA6		2000	23
SA7	10	500	2.5
SA8		1000	5
SA9		2000	10

Fig. 1 (a) SEM micrograph and (b–e) corresponding EDS maps for non-SMATed Mg5Zn0.2Ca alloy

in the micrographs). The darker appearance of the near-surface region increases in the optical micrographs with an increase in ball velocity, which occurs due to a transition from a coarser twin morphology to finer twins when comparing SA3 to SA9. The thickness of the SMAT-affected layer influenced by the ball velocity and surface coverage is shown in Fig. 4. In SA9, the presence of twins is evident up to a maximum depth of around $3000 \pm 500 \, \mu m$ (Fig. 4). Conversely, the lowest depth up to which twins are observed is around $400 \pm 100 \, \mu m$ for SA1.

Figure 5(a) shows XRD patterns of SMATed and non-SMATed specimens. They evidence the domination of α-Mg. A minute peak of $Ca_2Mg_6Zn_3$ phase (which has a minor quantity compared to α-Mg: see Fig. 1) is evident in the non-SMATed specimen (amplified view of the relevant region of XRD is shown in the insert of Fig. 4). Peak broadening is observed in all SMATed specimens.

As shown in Fig. 5(b) and (c), crystallite size is determined by assessing the broadening of the XRD peaks and utilizing the Williamson–Hall method (Ref 18). Figure 5(b) shows the crystallite size near the specimens' treated surface. However, the variation of crystallite size across the cross section of SA3, SA6, and SA9 (for 2000% coverage) is displayed in Fig. 5(c). Crystallite size is influenced by surface coverage and colliding ball velocity (Fig. 5b). The higher the surface coverage and ball velocity, the better the microstructural refinement. The SA9 shows the smallest crystallites of ~25 nm, indicating maximum grain refinement. On the other hand, SA1 exhibits the largest crystallite size of ~31 nm for 2000% coverage, reflecting the lowest degree of grain refinement.

3.2 Microhardness Distribution

Figure 6(a) depicts the surface microhardness variation of the SMATed specimens. The highest microhardness value of

~118 $HV_{0.05}$ is observed at the SA9 specimen's surface, while the SA1 specimen reports the lowest surface hardness value of ~68 HV0.05. There is a ~109% (~2.1 times) increase in the microhardness of SA9 compared to the microhardness of non-SMATed specimens (~56 $HV_{0.05}$). The microhardness distribution across the cross section of SMATed specimens (SA3, SA6 and SA9) is demonstrated in Fig. 6(b). The microhardness gradient is observed in all the cases. As the distance from the SMATed surface increases, the microhardness value decreases, eventually reaching a plateaued trend. Figure 6(c) depicts a 3D plot generated using MATLAB illustrating the variation of surface microhardness concerning ball velocity and surface coverage. This plot depicts elevated microhardness values attributed to higher colliding ball velocities and surface coverages.

3.3 Residual Stress Distribution

To measure the residual stress in the SMAT-affected region, an XRD peak of $(203)_{\alpha\text{-hcp}}$ ($2\theta = 90.46°$) is selected. Figure 7(a) shows an example of such peaks corresponding to the 50 μm distance from the SMATed surface. The d-spacing versus $\sin^2(\psi)$ method is employed to estimate the distribution of residual stress within the SMATed layer (representative plots are shown in Fig. 7b). Data points of the graphical presentation confirm the negative slope (m) through fitted lines, which are used to calculate the residual stress (Ref 20). The peak position is also influenced by grain size, micro-texture, and the gradient structure resulting from SMAT.

Surface roughness has also been identified as a contributing factor to the formation of residual stress (Ref 21). The surface roughness (R_a) values measured using a 2D profilometer indicate that the ball velocity considerably alters the surface roughness. It increases from 0.290 ± 0.012 to
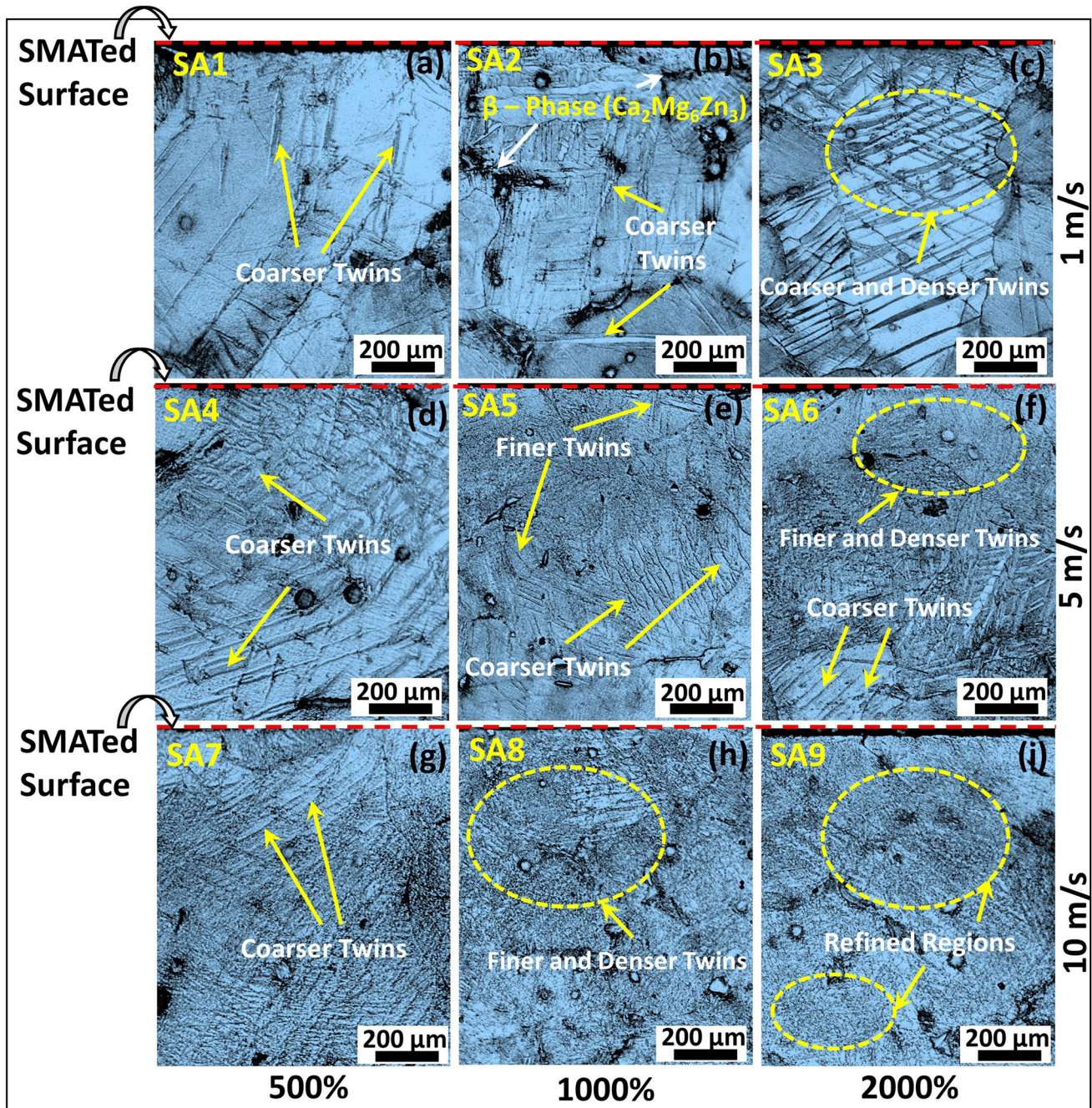
Fig. 2 (a–i) Microstructure of SMATed Mg5Zn0.2Ca alloy obtained using an optical microscope for different SMAT velocities and surface coverages

1.522 ± 0.043 μm with an increase in ball velocity from 1 to 10 m/s (at a 2000% coverage). However, surface coverage moderately alters the roughness, where a slight decrease in R_a value is observed from 1.783 ± 0.072 to 1.522 ± 0.043 μm with an increase in surface coverage from 500 to 2000% (at a 10 m/s ball velocity). Even though surface roughness influences the local stress concentration and subsequent relaxation behavior within a material, quantifying the effect of surface roughness on the residual stresses developed within the material is intricate. Numerous parameters within the stress relaxation mechanism (Section 4.3) add to this complexity.

The following expression is used to calculate the residual stress (Ref 22, 23):

$$\sigma_R = m \frac{E}{(1+v)} \qquad \text{(Eq 1)}$$

where σ_R is residual stress, v is Poisson's ratio, and E is Young's modulus for magnesium alloy. In this study, the considered elastic constants are a Poisson's ratio of 0.35 and an elastic modulus of 46 GPa (Ref 24). The SMATed specimens show compressive residual stresses generated at the surfaces (Fig. 7) and within the SMAT-affected layer (Fig. 8).

Figure 7(c) and (d) and a 3D plot (Fig. 7e) generated using MATLAB show the surface residual stress variation at different ball velocities and surface coverages. In a 3D plot (Fig. 7e), the
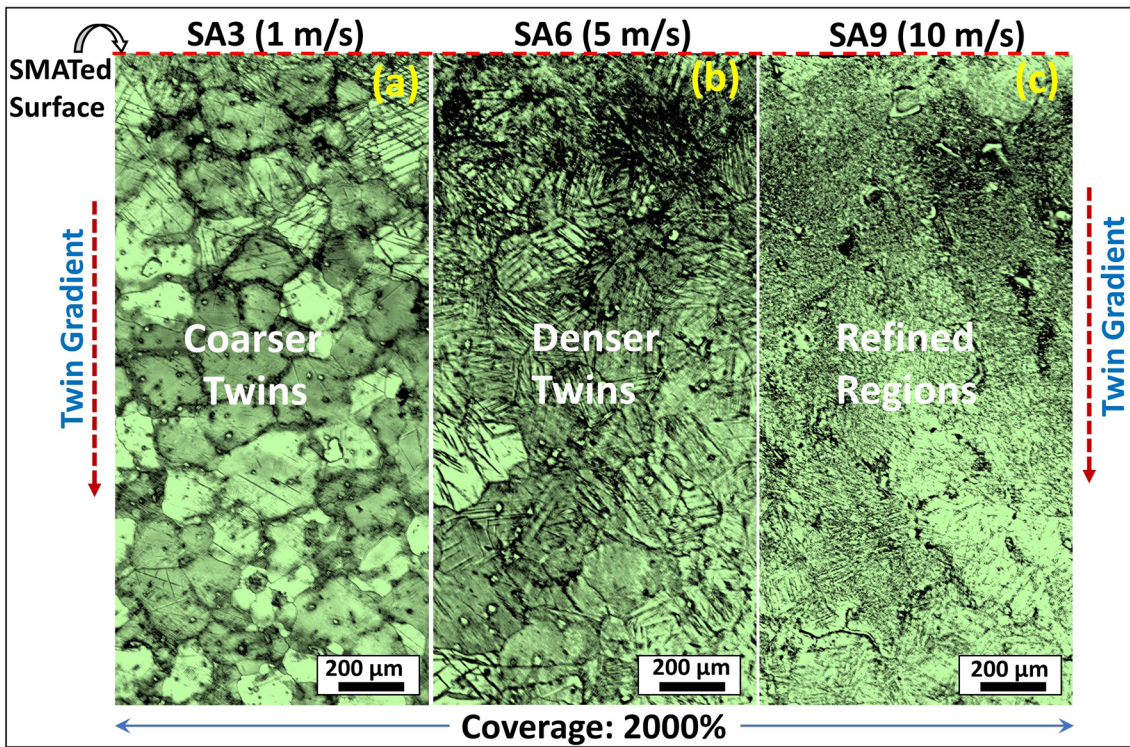
Fig. 3 Optical micrographs showing twin gradients across the cross section of (a) SA3, (b) SA6, and (c) SA9 at a constant surface coverage of 2000%
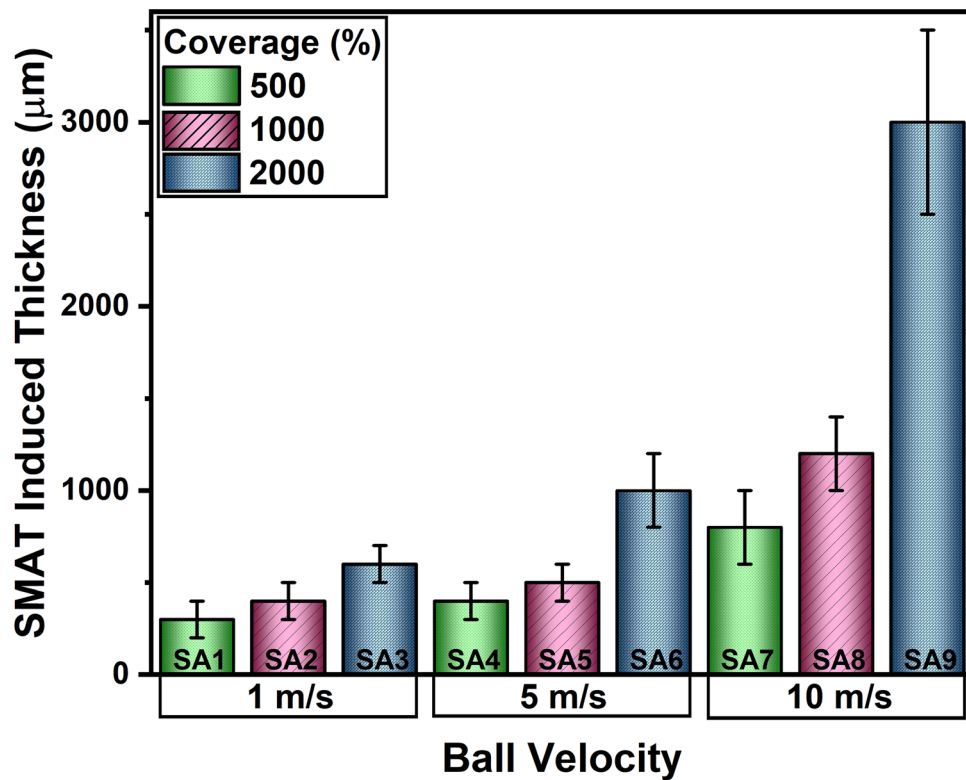

Fig. 4 Thickness of SMAT-affected regions for all specimens SMATed at different velocities of colliding balls and surface coverages.
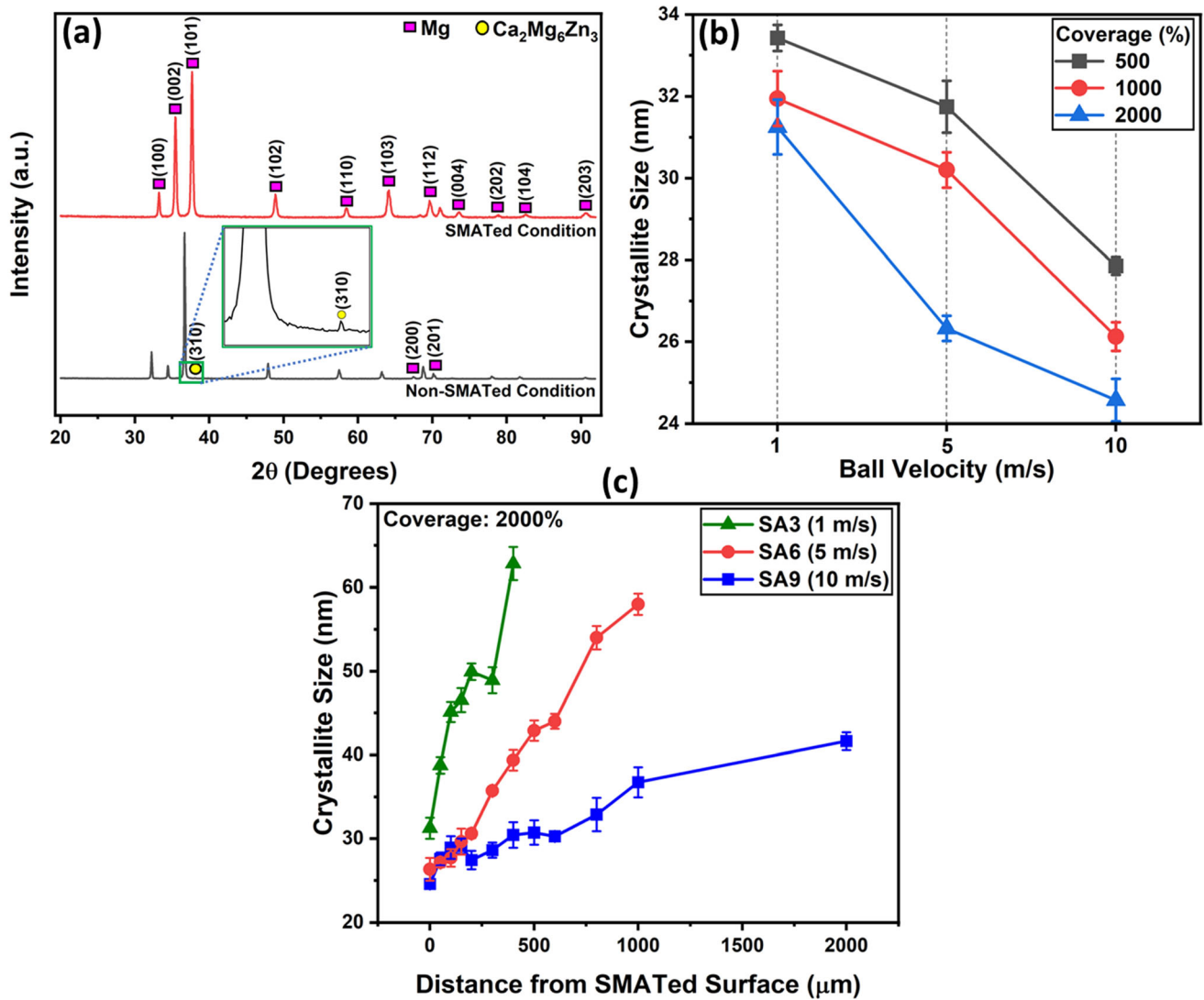
Fig. 5 (a) XRD patterns for non-SMATed and SMATed specimens, (b) Variation in crystallite size at SMATed surface for all specimens. (c) Crystallite size distribution within the SMATed layer (for SA3, SA6 and SA9) at a constant surface coverage of 2000%

R^2 value of ~0.96 ensures the closeness of fit. Hence, this profile illustrates a continuous and smooth transition without undulations across various surface coverages and ball velocities. This plot also highlights that higher surface coverage leads to a reduction in compressive residual stress values. However, there is an initial increase in residual stress magnitude with higher ball velocity, followed by a subsequent decrease as ball velocity continues to rise.

Notably, the specimens SMATed with a ball velocity of 5 m/s exhibit the highest (among the different ball velocities) amount of surface compressive residual stress for all surface coverages. Maximum compressive residual stress values at the surface are observed at 500% coverage for all ball velocities. The highest surface compressive residual stress of -153.5 ± 4.2 MPa is observed for SA4 (5 m/s ball velocity and 500% coverage). For a given ball velocity, residual stress becomes less compressive with an increased surface coverage (Fig. 7d), suggesting an increased resistance to the accumulation decrease in locked-in stress at the specimen surface with an increase in the SMATed layer thickness (Fig. 4) or an increase in the SMAT duration.

Figure 8(a), (b) and (c) demonstrates the residual stress distribution across the cross section for SA3, SA6, and SA9 at 2000% surface coverage. At some distance from the SMATed surface, the maximum compressive residual stress is observed. As the distance increases away from such depth toward the surface and core (i.e., non-SMATed region of the cross section), compressive residual stress decreases. The extent to which this decrement occurs toward the surface depends on the depth corresponding to the maximum compressive stress and the magnitude of this stress. SA3 and SA6 show the highest compressive stress almost at a similar distance from the surface (i.e., ~100 μm). However, SA6 has a higher magnitude of compressive stress $(-163.3 \pm 4.7$ MPa) than SA3 $(-73.1 \pm 5.1$ MPa) due to the higher kinetic energy of colliding balls (which is linked to the higher velocity of the balls). In other words, about the same volume of material (due to the similar depth of ~100 μm) closer to the SMATed surface experiences more accumulation of compressive stress for the SA6 than SA3. However, as the depth corresponding to the maximum compressive stress increases considerably, a near-surface region experiences lower compressive stress (even if
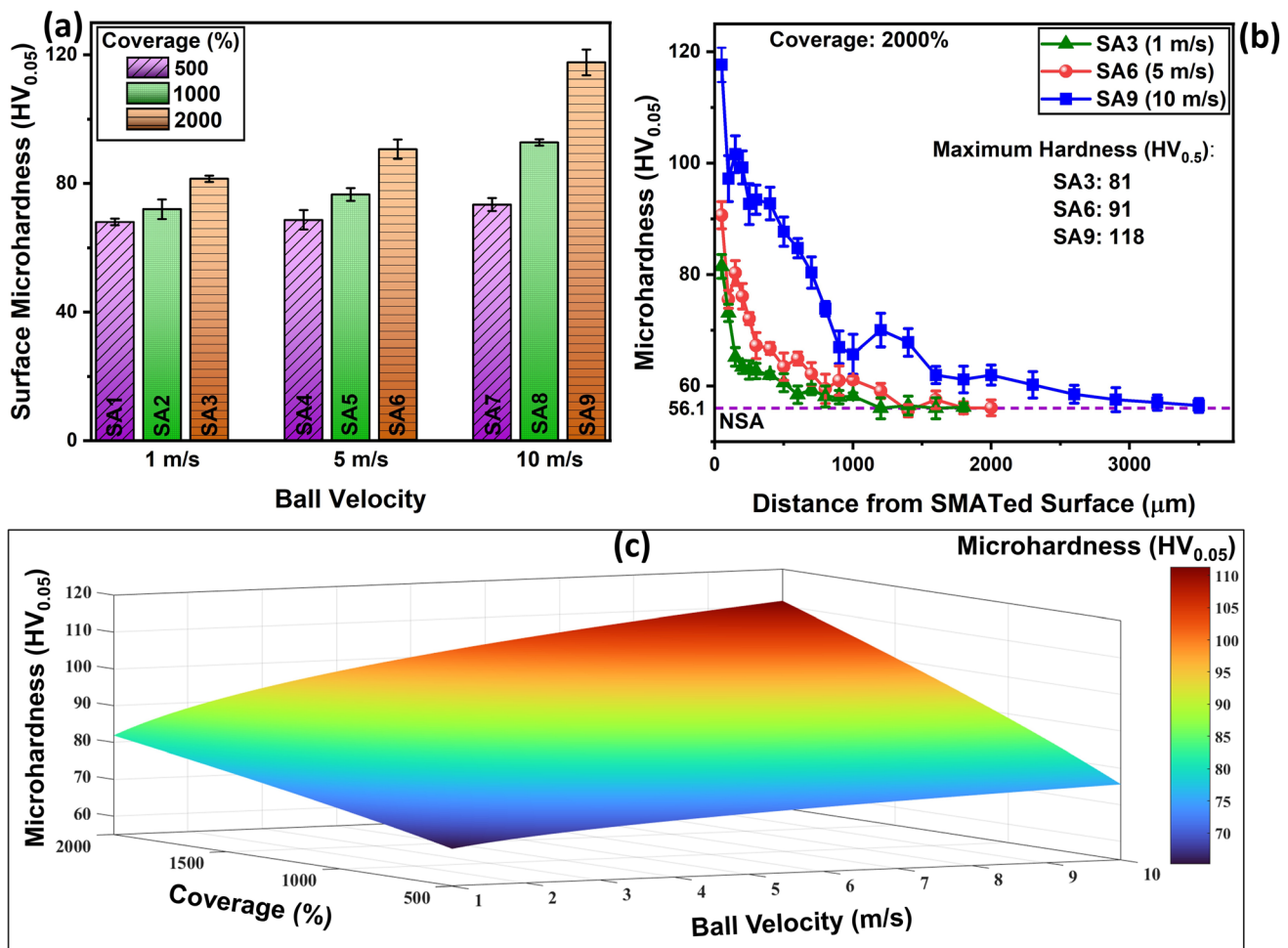
Fig. 6 (a) Surface microhardness variation for the SMATed specimens. (b) Microhardness gradient across the cross section of SA3, SA6 and SA9. (c) A 3D plot representing the variation in surface microhardness of the specimens SMATed at different ball velocities and surface coverages

the maximum compressive stress is somewhat higher). The SA9 specimen shows the highest magnitude of compressive residual stress (-175.5 ± 7.6 MPa) at ~ 600 μm depth. This magnitude of maximum stress is close to that of SA6 (-136.3 ± 4.7 MPa); however, the residual surface stress of SA9 is lower than SA6 (due to the substantially higher relevant depth: ~ 600 versus ~ 100 μm).

Mg5Zn0.2Ca alloy subjected to SMAT with a ball velocity of 5 m/s (SA6, SA5, and SA4) exhibits a thinner SMATed layer (Fig. 4) but notably higher surface compressive residual stress (Fig. 7) and optimal surface hardness (Fig. 6). However, the specimen treated at 10 m/s ball velocity exhibits the thicker SMAT-induced layer, high surface hardness, and maximum compressive residual stress in the layer. Consequently, SMAT processing of this alloy holds promise for further exploration and potential utilization in commercial applications.

4. Discussion

4.1 Microstructure Analysis

An intermetallic compound $Ca_2Mg_6Zn_3$ is evidenced in the microstructure of non-SMATed Mg5Zn0.2Ca alloy that is the

primary form of Zn in the α-Mg matrix (Fig. 1a). As shown in EDS maps (Fig. 1b–e), the distribution of Zn and Ca spans across the α-Mg phase. Notably, Zn and Ca exhibit a higher concentration along the grain boundaries. During the solidification of the MgZnCa alloy, the formation of α-Mg grains is followed by the enrichment of the boundaries with Zn and Ca (as the solubility of these elements is limited in α-Mg (Ref 25) leading to the precipitation of $Ca_2Mg_6Zn_3$ particles. Such microstructure evolution results in a higher concentration of Zn and Ca in the grain boundary regions. The phase proportion of $Ca_2Mg_6Zn_3$ in the microstructure is $\sim 2.2\%$. The precipitation of $Ca_2Mg_6Zn_3$ significantly influences the properties of the α-Mg alloy. These secondary phase particles act as obstacles to dislocation movement, especially at the grain boundaries, enhancing the alloy's overall strength (Ref 26).

The influence of increased ball velocities during SMAT on the microstructure is observed for constant surface coverage (Fig. 2a–i). For example, with a surface coverage of 2000%, SA9 demonstrates a higher twin density than SA6 and SA3, suggesting a higher degree of deformation of the specimens' surface due to the increased strains and strain rates generated by the higher velocity of colliding balls. Under constant ball velocity conditions, such as 1 m/s (Fig. 2a–c), SA3 (2000% coverage) exhibits denser twins compared to SA2 (1000%
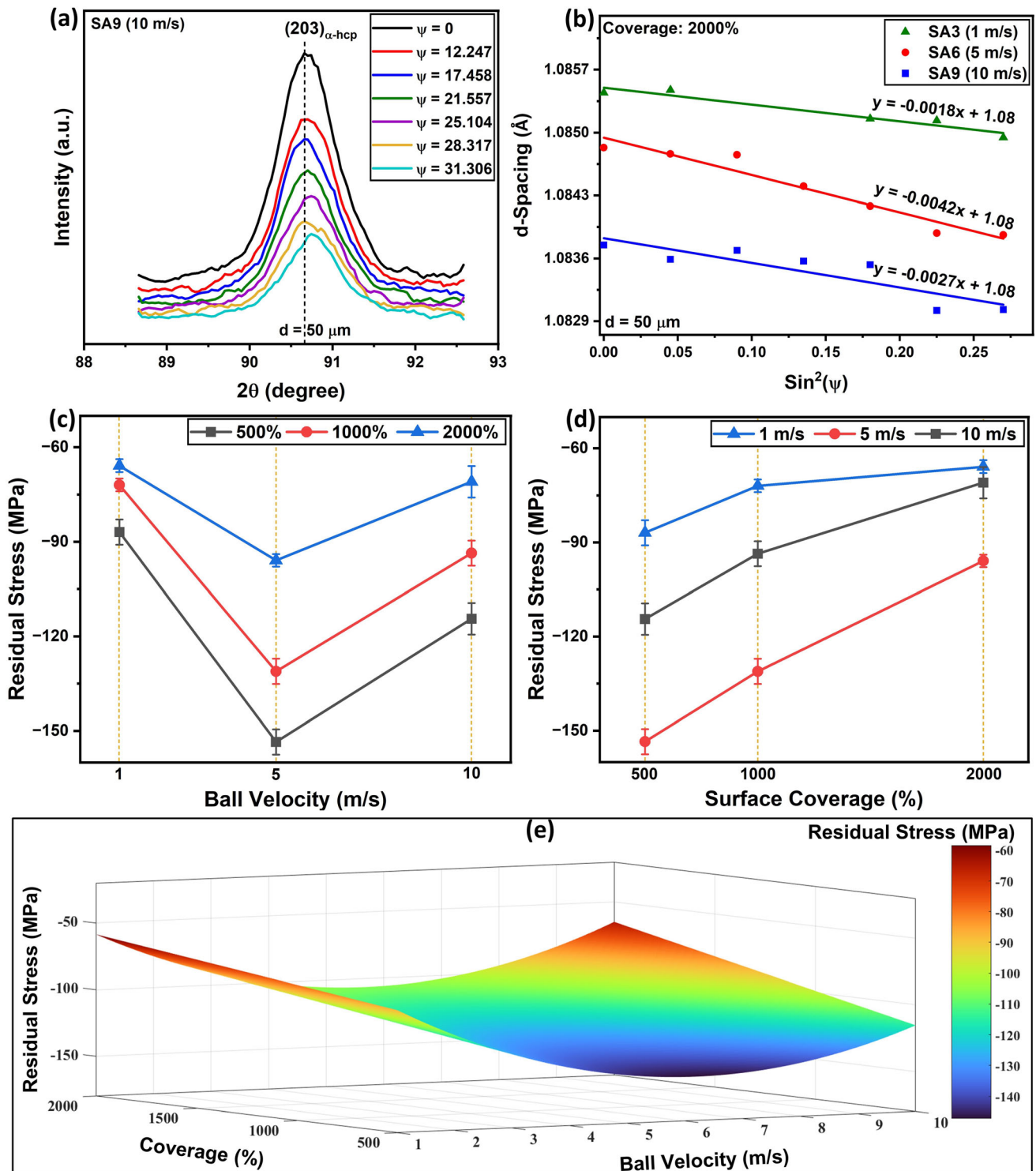
Fig. 7 (a) $(203)_{\alpha\text{-hcp}}$ XRD peaks of SA9 recorded at 50 μm depth. (b) d-spacing vs. $\sin^2(\psi)$ plot at 50 μm depth for SA3, SA6 and SA9. (c) (d) Surface residual stresses for the SMATed specimens. (e) A 3D plot representing residual surface stress distribution at different ball velocities and surface coverages

coverage) and SA1 (500% coverage). These consequences are attributed to an increased dislocation activity due to higher ball velocities and an increased percentage coverage.

Since magnesium alloy is an hcp material, dislocation slip and twinning are the predominant deformation mechanisms. This behavior can be further attributed to its low stacking fault energy. Initially, the impact of colliding balls during SMAT

significantly enhances the strain and strain rate in the region near the specimens' surface. Prolonged SMAT duration enables the colliding balls to penetrate deeper into the material, leading to an increased thickness of the SMAT-affected layer and even greater strains and strain rates in those regions. As a result of increased strain in the material, the movement of the dislocations occurs, leading to plastic deformation (Ref 27-30). When
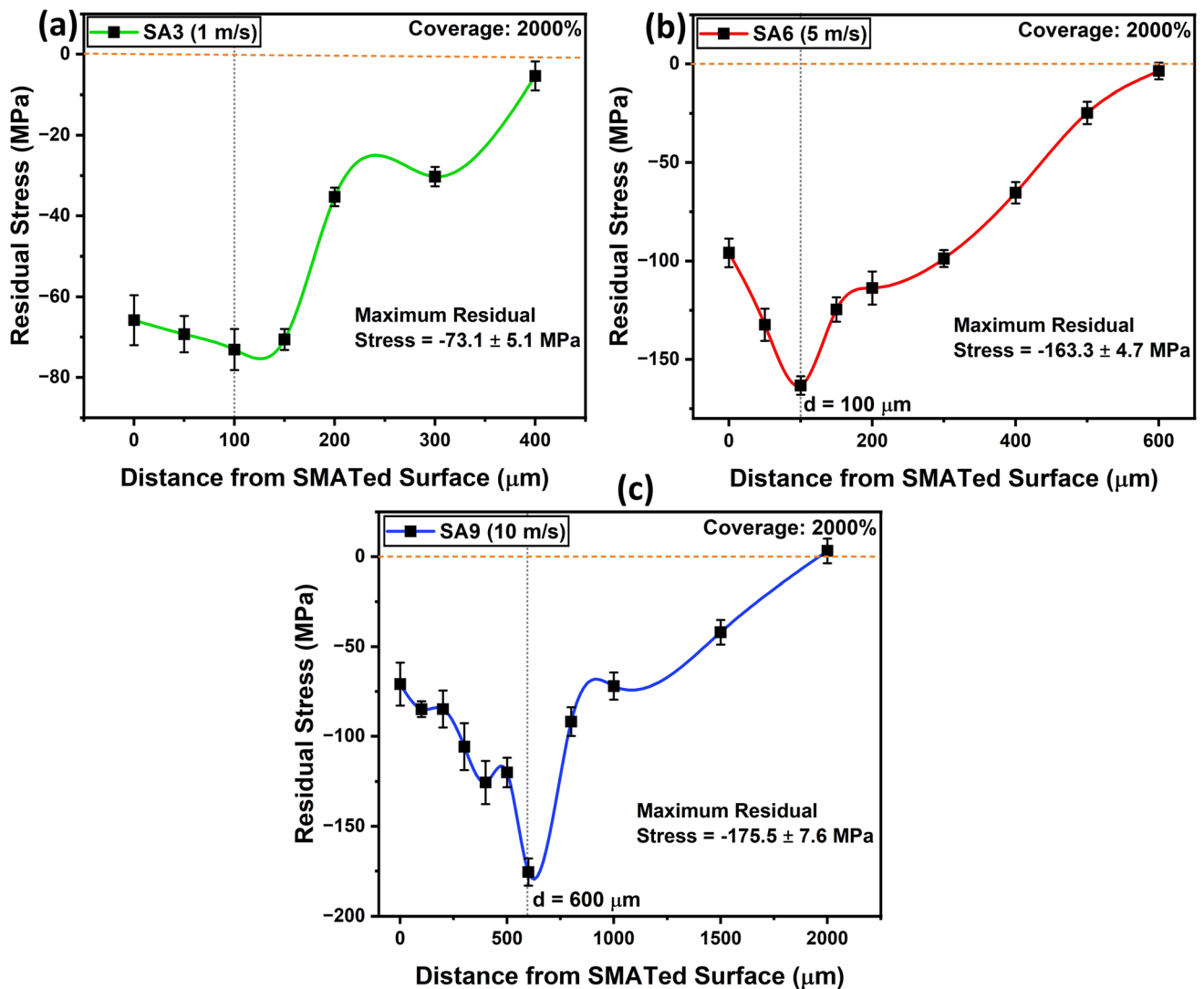
Fig. 8 (a) Distribution of residual stress across the cross section of (a) SA1, (b) SA4, and (c) SA7

a material deforms, strain and stress are not uniformly distributed across the cross section, and variations can occur in areas where they concentrate/localize. Consequently, non-uniformly distributed dislocations and twins can readily be observed.

The density of fine twins progressively reduces with an increased distance from the SMATed surface (Fig. 3a–c), and eventually, coarser twins form in the deeper regions. Strain variations and underlying microstructural changes across the material during deformation are the probable reasons for twin gradients (Ref 31, 32). However, the higher thickness of the SMAT-affected region as in the case of the SA9 specimen (Fig. 4) can be attributed to the higher impact energies and the increased deformation rate.

As shown in Fig. 5(a), a peak broadening is observed for the XRD peaks after SMAT and lattice defects, strain accumulation, and grain refinement are the major reasons for that. The smaller crystallite size (Fig. 5b) often reflects the broader diffraction peaks; hence, peak broadening indicates the nanocrystalline nature of materials (Ref 33, 34). Conversely, the crystallite size gradually increases from the SMATed surface to the core (Fig. 5c). In other words, the SMAT-affected regions of all the

SMATed specimens exhibit gradient structure concerning the crystallite size. It indicates that the variations in crystallite size can be attributed to the complex interaction among dislocations and twins and their density gradients (Fig. 2 and 3).

Due to the low shear stress requirements, the basal plane (0001) is the primary slip plane in magnesium alloys. Dislocations can serve as nucleation sites for twin formation, and the stress concentrations around them can facilitate the initiation and propagation of twinning deformations (Ref 31). As stain and strain rate increase (due to the increased ball velocity, percentage coverage, or SMAT duration), the density of dislocations increases, which interacts with twins and twin boundaries. These interactions between dislocations and twins influence the overall deformation behavior of the alloy. Dislocations can either pile up at twin boundaries (leading to their pinning) or glide through twin boundaries (causing their motion) (Ref 35). A higher density of dislocations and their interaction with twin boundaries further promotes twin formation, leading to dislocation-twin and twin-twin interactions. Consequently, the larger grains undergo fragmentation/division, leading to a refinement in grain size. Hence, due to comparatively higher strain and strain rates caused by a ball velocity of

10 m/s, SMATed specimens (SA7, SA8, and SA9) experience better grain refinement.

4.2 Microhardness Distribution

The gradient in microhardness (Fig. 6a and b) and fluctuations in the microhardness profiles could be linked to the variation in the density of crystal defects (like twins and dislocations) in the specimen cross section (Fig. 3). From a 3D plot (Fig. 6c), an empirical relationship is established for surface microhardness by fitting the profile as a function of ball velocity and surface coverage. The R^2 value of ~0.91 ensures the closeness of fit. Therefore, this profile demonstrates a smooth transition without any fluctuations across various surface coverages and ball velocities. The following equation expresses the established empirical relationship:

$$H_S = H_0 + V^{1/3}C^{3/4} \qquad \text{(Eq 2)}$$

where H_S is the surface microhardness, H_0 is the initial microhardness, V is the ball velocity (m/s), and C is the surface coverage (%). This equation indicates an increased microhardness value with an increased colliding ball velocity and surface coverage. However, from Eq 2, it is clear that surface coverage is a more dominating parameter than the colliding ball velocity. The presence of lattice defects, strain hardening, and grain refinement are the most probable reasons for increased hardness value after deformation.

Increasing dislocation activity (due to SMAT) allows more significant strain hardening and better grain refinement (Ref 27). The effect of grain size on hardness could be linked to the Hall–Petch relation (Ref 36). Due to the hcp crystal structure, magnesium alloys have inadequate slip systems and a larger Taylor factor (Ref 37), influencing the material constant (k) in the Hall-Petch equation and increasing the sensitivity of hardness value on grain size.

4.3 Residual Stress Distribution

The main cause of residual stress generation (Fig. 7a and 8) and variation (Fig. 7e) is the resistance encountered by the material during plastic deformation. Further, this behavior can be attributed to dislocation generation/accumulation, twin density, strain gradients, and grain refinement (Ref 38). Scattered data points observed in Fig. 7(b), which can be attributed to the x-ray penetration depth (Ref 20). Variations in ball velocities and surface coverages during SMAT notably impact several critical aspects of the material's behavior. Specifically, they influence the degree of grain refinement (Fig. 5), twins' distribution and density (Fig. 2 and 3), dislocation loops' formation, and the non-uniform strain distribution. This collective influence subsequently extends to the fluctuations in the magnitude of compressive residual stress that develops within the material and the intricate mechanism through which this stress relaxes over time (Ref 39-41). In the case of increased surface coverage for a given ball velocity, an increase in the SMATed layer thickness (Fig. 4) or an increase in the SMAT duration could relax the locked-in surface stress (Fig. 7d). Such relaxation in surface stress is possible at a constant surface coverage if ball velocity increases beyond a certain limit (Fig. 7c).

The material attempts to relax and reach equilibrium after the complete deformation process. The material, however, is in a metastable state due to the non-uniform distribution of strain and defects (Ref 39, 42). This response results in the generation of residual stress. Stress accumulation and defects near the deformed surface prevent the material from relaxing and increase residual stresses. In the presence of dislocations, twins, and grain boundaries, the stress is locked in the material and hinders it from completely relaxing (Ref 39-41). Hence, due to the non-uniform distribution and accumulation of strain during the deformation process, residual stress is often higher beneath the deformed surface (Ref 44).

The dependency of the residual surface stress on the ball velocity (which governs the kinetic energy of colliding balls) for a given surface coverage indicates the role of the amount of strain accumulation in the SMATed layer. When the value of maximum compressive residual stress is higher, but it occurs at a similar depth, about the same volume of material (due to the similar depth) closer to the SMATed surface experiences more accumulation of compressive stress due to the higher ball velocity (Fig. 8a versus b). Nevertheless, if the depth corresponding to the maximum compressive stress increases considerably, a near-surface region experiences lower compressive stress (Fig. 8b versus c). Moreover, the surface stress variation depends on the residual stress distribution across SMATed specimens and the stress relaxation phenomenon (Ref 39, 40, 42, 43). Therefore, the residual surface stress is a complex function of the cross-sectional width of the SMAT-affected region, surface coverage (which is also linked to the SMAT duration), the amount of maximum residual stress in the SMATed layer, and the depth at which the maximum residual stress accumulates.

Compressive residual stress typically enhances the resistance to deformation and failure of materials (Ref 44). It increases fatigue resistance and extends the material's service life by counteracting tensile stresses, which otherwise can initiate and propagate cracks (Ref 45). Especially in high-stress environments, compressive residual stress helps prevent premature failure and prolongs component durability.

5. Conclusions

This study investigates the impact of SMAT process parameters on the microstructure, microhardness, and residual stress of Mg5Zn0.2Ca magnesium alloy. Specimens SMATed with different ball velocities (1, 5, and 10 m/s) and surface coverages (500, 100, and 2000%) are examined to comprehensively explore the relationships between the SMAT parameters and their influence on the final material properties. The following are some major concluding remarks:

1. SMAT forms a layer with a gradient in hardness, crystallite size, and twins. The microhardness increases with an increased colliding ball velocity and surface coverage. Here, surface coverage is a more influencing parameter than the colliding ball velocity. The surface hardness value ranges between 68 and 118 $HV_{0.05}$, which is higher than the hardness of non-SMATed specimens (~56 $HV_{0.05}$).
2. SMAT induces compressive residual stress in the alloy's surface layer. The highest compressive residual is observed at some distance from the SMATed surface. As the distance increases from such depth toward the surface and core, the compressive residual stress decreases. High

ball velocity (10 m/s) and surface coverage (2000%) induce high compressive residual stress of about -175.5 MPa at ~ 600 μm depth. It is observed that the residual surface stress depends on the magnitude of maximum residual stress in the SMATed region and the depth at which maximum residual stress accumulates. Among the different ball velocities, the specimens SMATed with a ball velocity of 5 m/s exhibit the highest compressive residual stress at the surface for all surface coverages. The maximum surface compressive residual stress of about -153.5 MPa is observed for the specimens SMATed at 5 m/s ball velocity and 500% coverage.

3. The overall analysis reveals that the specimen treated at 10 m/s ball velocity and 2000% surface coverage exhibits the most refined grain structure, finely and densely distributed twins, maximum SMAT-induced thickness (~ 3000 μm), highest surface hardness (~ 2.1 times the hardness of non-SMATed specimen), and highest compressive residual stress at a certain distance away from the surface.

Acknowledgment

Competing interest

The authors declare that they have no known competing financial interests or personal relationships that could have appeared to influence the work reported in this paper

References

1. T. Zhang, W. Wang, J. Liu, L. Wang, Y. Tang, and K. Wang, A Review on Magnesium Alloys for Biomedical Applications, *Front. Bioeng. Biotechnol.*, 2022, **10**, p 953344. https://doi.org/10.3389/fbioe.2022.953344

2. Y. Sun, B. Zhang, Y. Wang, L. Geng, and X. Jiao, Preparation and Characterization of a New Biomedical Mg-Zn-Ca Alloy, *Mater. Des.*, 2012, **34**, p 58–64. https://doi.org/10.1016/j.matdes.2011.07.058

3. S. Nandy, S.P. Tsai, L. Stephenson, D. Raabe, and S. Zaefferer, The Role of Ca, Al and Zn on Room Temperature Ductility and Grain Boundary Cohesion of Magnesium, *J. Magnes. Alloy*, 2021, **9**(5), p 1521–1536. https://doi.org/10.1016/j.jma.2021.03.005

4. P. Makkar, S.K. Sarkar, A.R. Padalhin, B.G. Moon, Y.S. Lee, and B.T. Lee, In Vitro and in Vivo Assessment of Biomedical Mg-Ca Alloys for Bone Implant Applications, *J. Appl. Biomater. Funct. Mater.*, 2018, **16**(3), p 126–136. https://doi.org/10.1177/2280800017750359

5. I.P. Nanda, M.H. Hassim, M.H. Idris, M.H. Jahare, S.S. Abdulmalik, and A. Arafat, Mechanical and Degradation Properties of Zinc Adopted Magnesium Alloys for Biomedical Application, *IOP Conf. Ser. Mater. Sci. Eng.*, 2019 https://doi.org/10.1088/1757-899X/602/1/012094

6. P. Jiang, C. Blawert, R. Hou, J. Bohlen, N. Konchakova, and M.L. Zheludkevich, A Comprehensive Comparison of the Corrosion Performance, Fatigue Behavior and Mechanical Properties of Micro-Alloyed MgZnCa and MgZnGe Alloys, *Mater. Des.*, 2020, **185**, p 108285. https://doi.org/10.1016/j.matdes.2019.108285

7. V.E. Bazhenov, A.V. Li, A.A. Komissarov, A.V. Koltygin, S.A. Tavolzhanskii, V.A. Bautin, O.O. Voropaeva, A.M. Mukhametshina, and A.A. Tokar, Microstructure and Mechanical and Corrosion Properties of Hot-Extruded Mg-Zn-Ca-(Mn) Biodegradable Alloys, *J. Magnes. Alloy*, 2021, **9**(4), p 1428–1442. https://doi.org/10.1016/j.jma.2020.11.008

8. X. Yao, J. Tang, Y. Zhou, A. Atrens, M.S. Dargusch, B. Wiese, T. Ebel, and M. Yan, Surface Modification of Biomedical Mg-Ca and Mg-Zn-Ca Alloys Using Selective Laser Melting: Corrosion Behaviour, Microhardness and Biocompatibility, *J. Magnes. Alloy*, 2021, **9**(6), p 2155–2168. https://doi.org/10.1016/j.jma.2020.08.011

9. T.O. Olugbade, B.O. Omiyale, and O.T. Ojo, Corrosion, Corrosion Fatigue, and Protection of Magnesium Alloys: Mechanisms, Measurements, and Mitigation, *J. Mater. Eng. Perform.*, 2022, **31**, p 1707–1727. https://doi.org/10.1007/s11665-021-06355-2

10. F.X. Qin, C. Ji, Z.H. Dan, G.Q. Xie, H. Wang, S.I. Yamaura, M. Niinomi, and Y. De Li, Corrosion Behavior of MgZnCa Bulk Amorphous Alloys Fabricated by Spark Plasma Sintering, *Acta Metall. Sin.*, 2016, **29**(9), p 793–799. https://doi.org/10.1007/s40195-016-0451-9. (**English Letters**)

11. X.N. Gu, S.S. Li, X.M. Li, and Y.B. Fan, Magnesium Based Degradable Biomaterials: A Review, *Front. Mater. Sci.*, 2014, **8**, p 200–218. https://doi.org/10.1007/s11706-014-0253-9

12. V. Kumar, A. Sharma, S.S. Hosmani, and I. Singh, Effect of Ball Size and Impact Velocity on the Microstructure and Hardness of Surface Mechanical Attrition-Treated 304L Steel: Experiment and Finite Element Simulations, *Int. J. Adv. Manuf. Technol.*, 2022, **120**(5–6), p 3251–3267. https://doi.org/10.1007/s00170-022-08978-8

13. Y. Xu, D. Meng, L. Jing, Y. Cheng, J. Jia, and W. Li, Grain Refinement, Texture Evolution, and Tensile Performance Improvement of AZ91D Magnesium Alloy Processed by Multi-Cycle Accumulative Back Extrusion, *Adv. Eng. Mater.*, 2023, **25**(4), p 2201084. https://doi.org/10.1002/adem.202201084

14. S. Anand Kumar, P. Satish Kumar, S. Ganesh Sundara Raman, and T.S.N. Sankara Narayanan, Influence of SMAT Parameters on Microstructural and Mechanical Properties of Al-Mg-Si Alloy AA 6061, *J. Mater. Eng. Perform.*, 2017, **26**(4), p 1947–1957. https://doi.org/10.1007/s11665-017-2612-z

15. M. Kasaeian-Naeini, M. Sedighi, and R. Hashemi, Severe Plastic Deformation (SPD) of Biodegradable Magnesium Alloys and Composites: A Review of Developments and Prospects, *J. Magnes. Alloy*, 2022, **10**, p 938–955. https://doi.org/10.1016/j.jma.2021.11.006

16. G. Chen, J. Gao, Y. Cui, H. Gao, X. Guo, and S. Wu, Effects of Strain Rate on the Low Cycle Fatigue Behavior of AZ31B Magnesium Alloy Processed by SMAT, *J. Alloys Compd.*, 2018, **735**, p 536–546. https://doi.org/10.1016/j.jallcom.2017.11.141

17. G. Chen, Y. Fu, Y. Cui, J. Gao, X. Guo, H. Gao, S. Wu, J. Lu, Q. Lin, and S. Shi, Effect of Surface Mechanical Attrition Treatment on Corrosion Fatigue Behavior of AZ31B Magnesium Alloy, *Int. J. Fatigue*, 2019, **127**, p 461–469. https://doi.org/10.1016/j.ijfatigue.2019.06.031

18. M. Duan, L. Luo, and Y. Liu, Microstructural Evolution of AZ31 Mg Alloy with Surface Mechanical Attrition Treatment: Grain and Texture Gradient, *J Alloys Compd*, 2020, **823**, p 153691. https://doi.org/10.1016/j.jallcom.2020.153691

19. C. Chang, S. Yue, W. Li, L. Lu, and X. Yan, Study on Microstructure and Tribological Behavior of the Selective Laser Melted MgZnCa Alloy, *Mater. Lett.*, 2022 https://doi.org/10.1016/j.matlet.2021.131439

20. M. Mahmoodi, M. Sedighi, and D.A. Tanner, Investigation of through Thickness Residual Stress Distribution in Equal Channel Angular Rolled Al 5083 Alloy by Layer Removal Technique and x-Ray Diffraction, *Mater. Des.*, 2012, **40**, p 516–520. https://doi.org/10.1016/j.matdes.2012.03.029

21. J.N. Dastgerdi, F. Sheibanian, H. Remes, H.H. Toudeshky, and J. Barton, Influences of Residual Stress, Surface Roughness and Peak-Load on Micro-Cracking: Sensitivity Analysis, *Metals*, 2021, **11**(2), p 320. https://doi.org/10.3390/met11020320

22. Q. Chen, W.G. Mao, Y.C. Zhou, and C. Lu, Effect of Young's Modulus Evolution on Residual Stress Measurement of Thermal Barrier Coatings by x-Ray Diffraction, *Appl. Surf. Sci.*, 2010, **256**(23), p 7311–7315. https://doi.org/10.1016/j.apsusc.2010.05.071

23. C. Rathinasuriyan and V.S.S. Kumar, Experimental Investigation of Weld Characteristics on Submerged Friction Stir Welded 6061-T6 Aluminum Alloy, *J. Mech. Sci. Technol.*, 2017, **31**(8), p 3925–3933. https://doi.org/10.1007/s12206-017-0738-4

24. C. Moosbrugger, Engineering Properties of Magnesium Alloys, ASM International, 2017

25. J. Gao, J. Sharp, D. Guan, W. Rainforth, and L. Todd, New Compositional Design for Creating Tough Metallic Glass Composites with Excellent Work Hardening, *Acta Mater.*, 2015, **86**, p 208–215. https://doi.org/10.1016/j.actamat.2014.11.055

26. S. Du, K. Yang, M. Li, J.R. Li, Y.P. Ren, Q.Y. Huang, H.C. Pan, and G.W. Qin, Achieving High Strength above 400 MPa in Conventionally Extruded Mg-Ca-Zn Ternary Alloys, *Sci. China Technol. Sci.*, 2022, **65**(3), p 519–528. https://doi.org/10.1007/s11431-021-1911-3

27. M. Kavyani, G.R. Ebrahimi, H.R. Ezatpour, and M. Jahazi, Microstructure Refinement, Mechanical and Biocorrosion Properties of Mg-Zn-Ca-Mn Alloy Improved by a New Severe Plastic Deformation Process, *J. Magnes. Alloy*, 2022, **10**(6), p 1640–1662. https://doi.org/10.1016/j.jma.2020.11.013

28. S. Xia, Y. Liu, D. Fu, B. Jin, and J. Lu, Effect of Surface Mechanical Attrition Treatment on Tribological Behavior of the AZ31 Alloy, *J. Mater. Sci. Technol.*, 2016, **32**(12), p 1245–1252. https://doi.org/10.1016/j.jmst.2016.05.018

29. L. Zhang and Y. Han, Twins Formation and Their Role in Nanostructuring of Zirconium, *Mater. Sci. Eng. A*, 2009, **523**(1–2), p 130–133. https://doi.org/10.1016/j.msea.2009.05.057

30. N.K. Kumbhar, V. Kumar, D. Singh, and S.S. Hosmani, Gradient Microstructure and Properties of Surface Mechanical Attrition-Treated AZ91D Alloy: An Effect of Colliding Balls Velocity, *Adv. Eng. Mater.*, 2023 https://doi.org/10.1002/adem.202300549

31. X. Chen, C. Liu, Y. Wan, S. Jiang, X. Han, and Z. Chen, Formation of Nanocrystalline AZ31B Mg Alloys via Cryogenic Rotary Swaging, *J. Magnes. Alloy*, 2021 https://doi.org/10.1016/j.jma.2021.11.021

32. X. Meng, M. Duan, L. Luo, D. Zhan, B. Jin, Y. Jin, X. Xin Rao, Y. Liu, and J. Lu, The Deformation Behavior of AZ31 Mg Alloy with Surface Mechanical Attrition Treatment, *Mater. Sci. Eng. A*, 2017, **707**, p 636–646. https://doi.org/10.1016/j.msea.2017.09.094

33. D. Singh, D.A. Basha, L. Wadsö, D. Orlov, Y. Matsushita, A. Singh, and S.S. Hosmani, Evolution of Gradient Structured Layer on AZ91D Magnesium Alloy and Its Corrosion Behaviour, *J. Alloys Compd.*, 2021, **882**, p 160659. https://doi.org/10.1016/j.jallcom.2021.160659

34. X. Liu and R. Xu, Microstructure Evolution and Thermal Stability of Mg-Sm-Ca Alloy Processed by High-Pressure Torsion, *J. Mater. Eng. Perform.*, 2022, **31**(4), p 2644–2652. https://doi.org/10.1007/s11665-021-06433-5

35. C. Liu, X. Chen, Y. Hu, W. Zhang, Y. Zhang, J. Li, and F. Pan, Microstructure and Mechanical Properties of Gradient Ultrafine-Grained Mg-Gd-Zr Alloy, *J. Mater. Res.*, 2022, **21**, p 3896–3908. https://doi.org/10.1016/j.jmrt.2022.11.008

36. S.N. Naik and S.M. Walley, The Hall-Petch and Inverse Hall-Petch Relations and the Hardness of Nanocrystalline Metals, *J. Mater. Sci.*, 2020, **55**, p 2661–2681. https://doi.org/10.1007/s10853-019-04160-w

37. J.H. Shen, Y.L. Li, and Q. Wei, Statistic Derivation of Taylor Factors for Polycrystalline Metals with Application to Pure Magnesium, *Mater. Sci. Eng. A*, 2013, **582**, p 270–275. https://doi.org/10.1016/j.msea.2013.06.025

38. H. Liu, X. Wei, S. Xing, L. Wang, W. Zhu, C. Jiang, V. Ji, and K. Zhan, Effect of Stress Shot Peening on the Residual Stress Field and Microstructure of Nanostructured Mg-8Gd-3Y Alloy, *J. Mater. Res. Technol.*, 2021, **10**, p 74–83. https://doi.org/10.1016/j.jmrt.2020.11.085

39. Z. Trojanová, Z. Drozd, P. Lukáč, and J. Džugan, Stress Relaxation Tests: Modeling Issues and Applications in Magnesium Alloys and Composites, *J Mater. Eng. Perform.*, 2022 https://doi.org/10.1007/s11665-022-06951-w

40. F. Li, G. Chen, T. Dong, C. Zhu, and K. Chen, Microplastic Deformation Activating Residual Stress Relief for Al Alloy, *Int. J. Mech. Sci.*, 2023, **254**, p 108446. https://doi.org/10.1016/j.ijmecsci.2023.108446

41. J.S. Wang, C.C. Hsieh, H.H. Lai, C.W. Kuo, P.T.Y. Wu, and W. Wu, The Relationships between Residual Stress Relaxation and Texture Development in AZ31 Mg Alloys via the Vibratory Stress Relief Technique, *Mater. Charact.*, 2015, **99**, p 248–253. https://doi.org/10.1016/j.matchar.2014.09.019

42. W.Z. Zhuang and G.R. Halford, Investigation of Residual Stress Relaxation under Cyclic Load, *Int. J. Fatigue*, 2001, **23**, p 31–37.

43. M.X. Yang, R.G. Li, P. Jiang, F.P. Yuan, Y.D. Wang, Y.T. Zhu, and X.L. Wu, Residual Stress Provides Significant Strengthening and Ductility in Gradient Structured Materials, *Mater. Res. Lett.*, 2019, **7**(11), p 433–438. https://doi.org/10.1080/21663831.2019.1635537

44. A.R. Eivani, H. Vafaeenezhad, H.R. Jafarian, and J. Zhou, A Novel Approach to Determine Residual Stress Field during FSW of AZ91 Mg Alloy Using Combined Smoothed Particle Hydrodynamics/Neuro-Fuzzy Computations and Ultrasonic Testing, *J. Magnes. Alloy*, 2021, **9**(4), p 1304–1328. https://doi.org/10.1016/j.jma.2020.11.018

45. X. Song, W.C. Liu, J.P. Belnoue, J. Dong, G.H. Wu, W.J. Ding, S.A.J. Kimber, T. Buslaps, A.J.G. Lunt, and A.M. Korsunsky, An Eigenstrain-Based Finite Element Model and the Evolution of Shot Peening Residual Stresses during Fatigue of GW103 Magnesium Alloy, *Int. J. Fatigue*, 2012, **42**, p 284–295. https://doi.org/10.1016/j.ijfatigue.2012.01.019